Development of a wall shear stress integral measurement and analysis system for two-phase flow boundary layers

Elvis E. Dominguez-Ontiveros, Carlos E. Estrada-Perez, Javier Ortiz-Villafuerte,[a] and Yassin A. Hassan
Department of Nuclear Engineering, Texas A&M University, College Station, Texas 77843-3133

(Received 4 April 2006; accepted 12 September 2006; published online 17 October 2006)

An integral system was developed for the measurement and analysis of wall shear stress data from a two-phase boundary layer flow. Three different and independent measurement techniques are incorporated in a synchronized acquisition system. The three measurement techniques are the particle tracking velocimetry, a differential pressure transducer, and an optical wall shear stress sensor. Each of these techniques provides complementary information that helps in the description and understanding of the phenomena involved in a two-phase boundary layer. The practical implementation of the integral measurement and analysis system is demonstrated with the measurement of the wall shear stress of a microbubble laden boundary layer flow in a channel. The agreement in the results of the wall shear stress from the three synchronized measurements techniques was 93% for the single-phase case and 92.8% for the two-phase flow measurements. Moreover, independent measurements with each technique show no appreciable change in the values obtained when they were all synchronized. The advantages and limitations of each individual technique are discussed for measurement and analysis of two-phase flow data, as well the advantages of having an integral system that combines the information from all measurement techniques at the same time. © *2006 American Institute of Physics.* [DOI: 10.1063/1.2360887]

I. INTRODUCTION

Wall shear stress is an important parameter for characterizing bounded and unbounded flows, especially in their boundary layers. Determining this parameter, also known as skin friction, is of primary significance for the study of theoretical and applied fluid mechanics. Its potential application is as broad as the fluid mechanics field, so it is not surprising to find researchers working in the biomedical field and dealing with similar challenges as naval engineers or aerospace engineers when quantification of wall shear stress is the topic of matter. The wall shear stress produced by a fluid flowing along a solid wall is a complex quantity to measure, especially when multiphase flows are considered.

A number of well-known techniques exist for measuring skin friction and can be broadly categorized as direct and indirect measurement techniques. Direct techniques are those in which the force (stress) on the wall is measured directly. Some examples of these methods are the floating element and the servo-force balance technique.[1] Direct measurement techniques are advantageous since they do not rely on theoretical or empirical data to obtain the shear stress. However, these techniques are often susceptible to noise from mechanical systems and require constant maintenance for optimum performance. Indirect techniques infer the skin friction from other quantities, such as heat transfer from a surface probe,[2,3] surface deformation of a sensing element,[4] sensing dynamic pressure in block probes,[5] or knowledge of the velocity components close to the wall. Indirect techniques are often more robust than direct methods, but they inherently rely on theoretical or empirical correlations to determine the shear stress.

Although several techniques exist for direct or indirect measurement of physical quantities in single-phase flows, few of them can be applied for the measurement or inference of the friction velocity or wall shear stress in a microbubble boundary layer. The injection of small diameter bubbles into the boundary layer has been studied as one method to achieve drag reduction. Microbubble boundary layers occur in diverse scenarios. One example is the use of microbubbles as agents that reduce the friction drag, or skin friction, which is responsible for almost all the friction retarding the movement of big ships or underwater vehicles. The design of transport systems that take advantage of drag reduction via microbubble injection in liquid boundary layers can lead to important energy savings and environmental protection.

Various drag reduction investigations have been performed with the injection of microbubbles. In most of these works, quantification of the wall shear stress has played an important role to determine the amount of success in achieving drag reduction. In 1973 Mccormick and Bhattacharyva[6] reported the first experimental work with the microbubble injection. They used a copper wire wound around a towed body to produce hydrogen bubbles by electrolysis. The effects of microbubbles on a turbulent boundary layer have also been studied by Migirenko and Evseev[7] and Bogdevich and Evseev.[8] Instead of using electrolysis to generate bubbles, these authors forced air through a porous surface with pore sizes ranging from 1 to 50 μm. Their experiments were conducted using a simple flat geometry and all mea-

[a]Currently at Instituto Nacional de Investigaciones Nucleares of México.

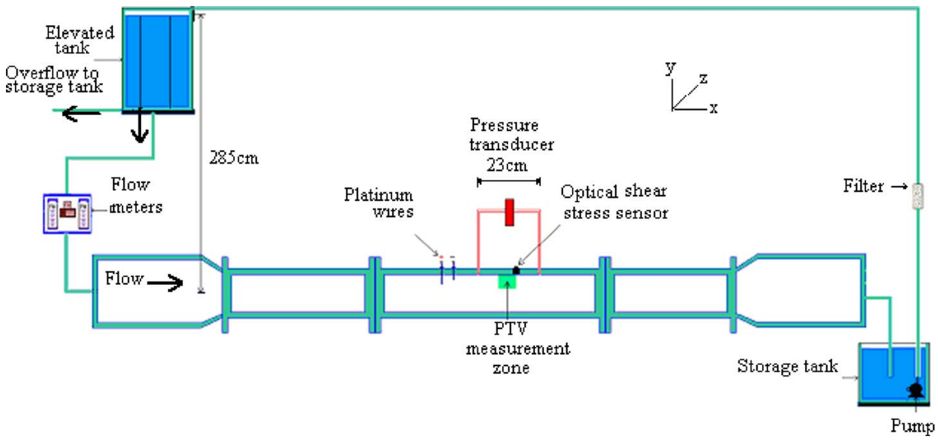

FIG. 1. (Color online) Schematic experimental setup of the hydraulic facility with sensors location.

surements were made downstream of the porous section. Drag reductions as high as 80% on flat plate boundary layers were achieved with the injection of microbubbles.[9] Moreover, Fontaine *et al.*[10] reported the achievement of more than 80% of drag reduction using a combination of polymers with microbubbles.

Recently, many researchers have reported drag reduction by injection of gas microbubbles.[11–13] In most of these experiments, gas is injected through a porous plate located inside the channel flow and the measurement of the drag is made by means of different techniques.

In this work, an integral system that allows the measurement of wall shear stress in microbubble laden boundary layers has been developed and implemented. The system has been tested on microbubble boundary layer in a turbulent channel flow. The system consists of three independent and synchronized measurement techniques that provide complementary information about the phenomena occurring in a liquid boundary layer disturbed by the presence of microbubbles. The three techniques are particle tracking velocimetry (PTV), measurement of the pressure gradient via an accurate differential pressure transducer, and direct measurements of the wall shear stress by an optical sensor. Measurements of wall shear stress are obtained in the channel flow for pure water and water with microbubble injection. Microbubbles (30 μm average diameter) are produced close to the measurement area by an electrolysis process. The microbubbles are injected within the buffer sublayer of the turbulent boundary layer, and their effect in the wall shear stress is quantified using the proposed measurement system. The three techniques show a decrease in the wall shear stress when the microbubbles are injected. The benefits of obtained data with reduced uncertainty by combining the techniques mentioned above and the potential to further clarify the role of shear stress in two-phase flows are presented.

II. EXPERIMENTAL SETUP

The experiment was carried out in a rectangular cast acrylic channel, with dimensions of 4.8 m in length, 20.6 cm in width, and 5.6 cm in height. Water was pumped through a closed loop. First water flowed from an elevated tank to the channel by gravity. Then, water was conducted to a storage tank from which water was pumped back to the elevated tank. The upper tank has a constant water head maintained by the pumps. A schematic diagram of the experimental setup is illustrated in Fig. 1 and a photograph of the components is shown in Fig. 2.

The velocity field in the X-Y plane is obtained by PTV at 3.15 m downstream from the channel inlet ($L/H = 315\ \mathrm{cm}/2.8\ \mathrm{cm} = 112.5$, where H is half the channel height). An Nd:YAG (yttrium aluminum garnet) laser with a wavelength of 532 nm (green light) and power of 350 mJ/pulse is utilized in the viewing area. The particle seeds used for tracing the flow have small diameters ranging from 6 to 9 μm and have a specific gravity of 1.01 which is close to that of water.

The scattered laser light from the seeding particles is recorded using a charge-coupled device (CCD) Kodak Megaplus camera, model ES 1.0, 1008×1018 pixels. The viewing area is 1.28 cm^2 and is located close to the upper channel's wall. The system records 30 velocity fields/s. Each velocity field is obtained from a pair of consecutive images spaced 1 ms apart via a frame straddling approach. Images were recorded for a time span of approximately 3.3 s.

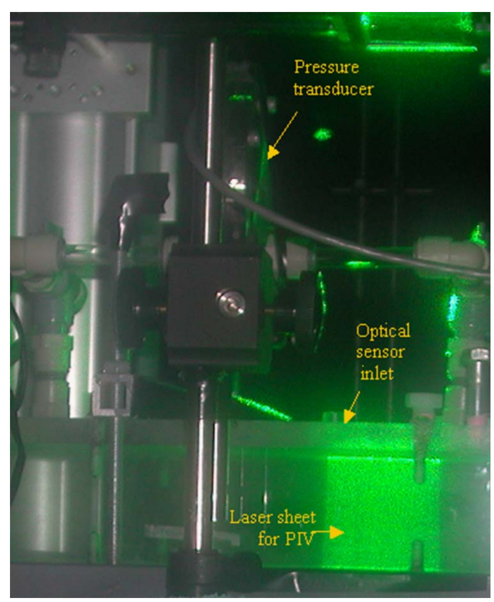

FIG. 2. (Color online) Photograph of the measurement system components (PTV measurement area, differential pressure sensor, and wall shear stress optical sensor).

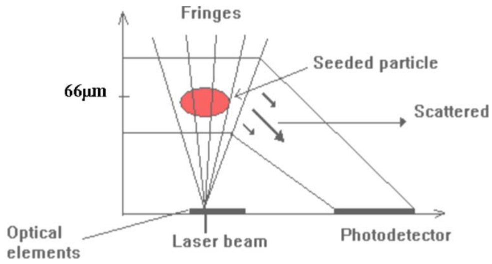

FIG. 3. (Color online) Schematic of the principle of operation for the optical shear stress sensor.

The pressure gradient in the test section was measured with pressure taps positioned on the top wall of the channel over a distance of 23 cm. A Validyne pressure transducer (model DP103) is used. This device utilizes a central diaphragm as a sensor element and is of the variable reluctance type. Because the diaphragm needs to move only one- or two-thousandths of an inch to produce a full-scale output, the thickness and area of the diaphragm determine the full-scale pressure range. A large diaphragm made of thin foil will respond to extremely low pressures. Conversely, a thick diaphragm with a small area responds to very high pressures. The transducer has a range of pressure difference from 0 to 35 ± 0.09 Pa. To obtain the wall shear stress from the pressure drop measurements of fully developed two dimensional single-phase channel flows, the following equation can be utilized:

$$\tau_w = -H\frac{\Delta P}{\Delta x}, \tag{2.1}$$

where τ_w is the wall shear stress, ΔP is the pressure drop measured by the pressure transducer, Δx is the axial distance between the pressure connection tabs, and H is the half-width of the channel.

An optical shear stress sensor was also used in the present study to measure wall shear stress fluctuations. The sensor's principle of operation is based on a measurement technique using divergence fringe Doppler theory. Its principle is very similar to the well-known laser doppler velocimetry (LDV). A laser beam is passed through an array of optical elements to obtain a divergent interference fringe pattern originated at the surface of the sensor and extending into the flow.[14] The scattered light from a particle passing through the fringes is collected through a window at the surface of the sensor and focused onto a multimode fiber by the receiver diffractive optical element.

The probe volume region is defined by the intersection of the transmitter and receiver fields centered at approximately 66 μm above the surface (see Fig. 3). Detailed information about the sensor specific characteristics is available in the literature.[15] The optical shear stress sensor system includes a low pass filter, which limits the frequency output of the burst produced by the particles crossing the Doppler fringes. One of the differences between the laser Doppler velocimetry and the optical shear stress sensor is that LDV uses a set of parallel fringes at the probe volume to measure the velocity, while the shear stress sensor uses a set of diverging fringes to measure the gradient of the velocity.

The fringe separation is specified by the micro-optical array located at the sensors' surface. This array separates the laser beam into various fringes that diverge linearly with the distance from the surface of the optical array, y. Since the divergence factor k is obtained from the lens characteristics inside the micro-optical array, it is a known specified by the fabricant. Hence the local fringe separation δ can be obtained by knowing the divergence factor and the distance from the micro-optical array,

$$\delta = k \times y. \tag{2.2}$$

The velocity of a particle crossing the measurement volume, u, is obtained from

$$u = f \times \delta, \tag{2.3}$$

where f is the Doppler frequency. The Doppler frequency multiplied by the fringe divergence factor yields the velocity gradient in the quasilinear sublayer of the boundary layer,

$$\frac{u}{y} = f \times k. \tag{2.4}$$

These expressions mean that the sensor measures the velocity at a distance of 66 μm from the micro-optical elements. These measurements are then used to obtain the velocity gradient, since the divergence factor of the fringes is known. Finally, the wall shear stress is obtained by multiplying the velocity gradient times the water viscosity μ.

The hydrogen microbubbles used to achieve drag reduction are produced by electrolysis located at 10 cm upstream from the test zone. Platinum wires with a diameter of 76 μm

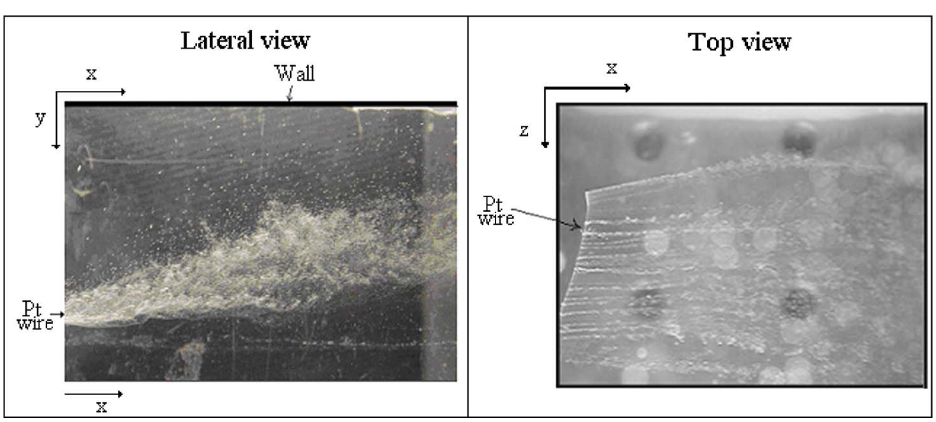

FIG. 4. Microbubble injection by electrolysis. The bubbles are injected into the buffer sublayer of the boundary layer with an average diameter of 30 μm.

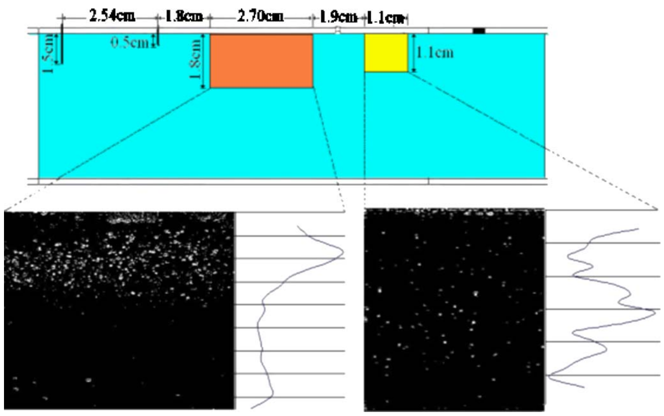

FIG. 5. (Color online) Experimental setup for measurement of microbubble distribution, Re=5128. Two cameras are placed perpendicular to the channel. The SPIV and PTV are combined to measure microbubble distribution. The distribution profiles are shown besides typical microbubble images.

are used as electrodes, as shown in Fig. 4. This figure presents the lateral and top views of the microbubble regime. It also delineates the microbubble sheet dispersion. To produce hydrogen microbubbles of 30 μm in diameter, a current of 25 mA is conducted through the electrodes. The negative electrode (cathode) produces hydrogen microbubbles, whereas the positive one (anode) produces oxygen microbubbles.

Bubbles' distribution and trajectories are obtained by using a hybrid shadow pulsed image velocimetry (SPIV) and PTV techniques. In classical shadowgraphy, a collimated beam of light wide enough to cover the entire flow region of interest is aimed across the flow and onto an imaging device. Any variation in the density of the flowing medium is accompanied by a variation in the refractive index and gives rise to a shadow, which alters the distribution of brightness of light striking the imaging device. Due to simplicity of this concept, shadowgraphs have been used with success in bubble interactions, two-phase flow, particle sizing, diagnosing shocks, and other flow phenomena. For our case, the shadowgraphy technique is implemented in conjunction with a pulsating illumination source and the resulted microbubbles' shadows tracked with PTV algorithms. In this way, the microbubbles distribution and trajectories are obtained within the turbulent boundary layer. In the microbubble distribution experimental setup, a complementary metal-oxide semiconductor (CMOS) camera model GPMF702 with 640×480 pixel resolution (camera 1) and a CCD camera model Megaplus ES1.0 of 1008×1008 pixel resolution (camera 2) are both placed perpendicularly to one side of the channel wall to record images in the *X-Y* plane. The camera's equivalent viewing areas are 2.7 cm in width $\times1.8$ cm in height for camera 1 and 1.1 cm in width $\times1.1$ cm in height for camera 2. The viewing areas of camera 1 and camera 2 will be referred as measurement area A and measurement area B, respectively, as illustrated in Fig. 5. It must be noticed that measurement area B is where the synchronization system is implemented later on. An example of the instantaneous bubbles present at each area can be observed from this figure. In both images can be appreciated that some of the bubbles are attached to the top wall of the channel. The plots at the right side of each image represent the average bubble distribution at their respective measurement zone for a Reynolds number equal to 5128. Measurement areas A and B are located at 1.8 and 6.4 cm downstream of the platinum electrode. The SPIV technique is used at measurement area A to determine bubbles' distribution and trajectories. At location B both SPIV technique and the particle tracking velocimetry (PTV) technique are employed to obtain the microbubble concentrations and instantaneous velocity field. The experiments are performed under a Reynolds number of 5128 based on half height of the channel and bulk velocity. Microbubble percentage distributions for this flow condition are shown in Fig. 6. Two distribution peaks are observed for measurement area B at distances of 1.1 and 6 mm from the top wall of the channel. By knowing the bubble distribution within the boundary layer, one can assure that the microbubble injection is taking place at the desired location. In this work, the effect of microbubble injection within the buffer sublayer of the channel's turbulent boundary layer is of relevance due to its drag reduction implications, and one important manifestation of this physical phenomenon is the reduction of the wall shear stress.

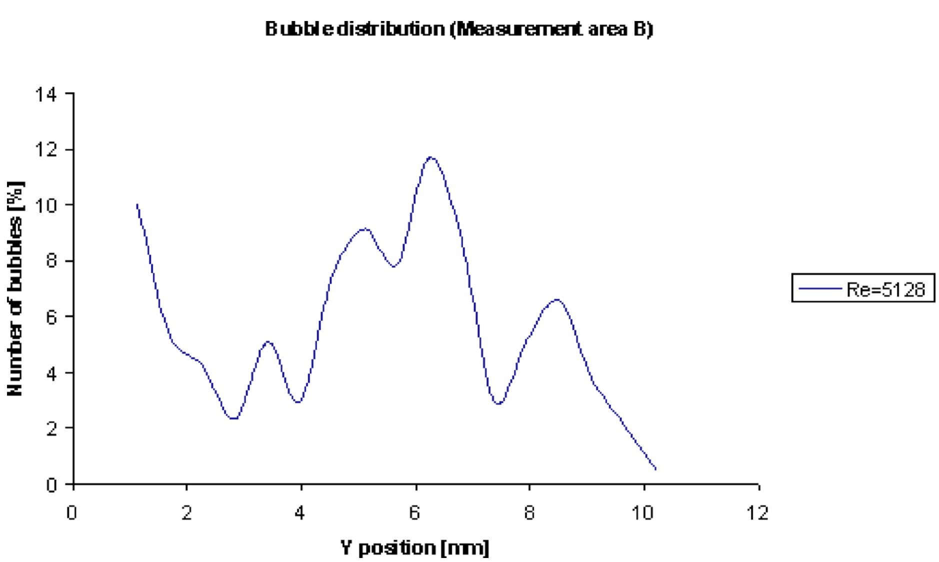

FIG. 6. (Color online) Microbubble percentage distribution, Re=5128. Two important distribution peaks are observed at 1 and 6 cm.

A. Synchronization

The term synchronization is referred as the ability to relate data to a single time frame. In other words, the time frame used during the experimentation can be related to almost all the equipments, used during the acquisition processes. This is of great help especially in the turbulence field where fluctuating parameters can be detected by one or more devices at the same instant of time and with thus decreasing the possibility of measurement error or wrong interpretation of the results.

The system will be described by following the sequence that the primary time generator follows to deliver synchronized pulses to the various devices.

B. Pulse generator

The pulse generator is the time base for the whole acquisition system. A high-accuracy pulse generator model DG535 fabricated by Stanford Research Systems Inc. generates the initial signal by means of an internal clock. This device has five output channels (A, B, C, D, and E) that can be configured to deliver an output signal based on specific time delays programed by the user. The internal clock was programed to run at a frequency of $T_0=30$ Hz. Channel A was programed to generate a short-time square pulse with a time delay of 0.165 ms after the falling edge of T_0. Channel C is generated with a time delay equal to the summation of time $T_0+B+0.165$ ms where B is the time delay programed for channel B. For this study the value of B was fixed to 1 ms and represents the time span between the two laser shots (Δt_{PIV}).

C. Laser

The twin laser lamps of the Nd:YAG laser can be triggered independently by sending a transitor-transitor logic (TTL) pulse to the corresponding trigger input of each lamp. The designated channels that drive the pulses for triggering the lamps are channel A for the first lamp and channel C for the second lamp of the laser in this particular case.

D. High-resolution camera

The high-resolution camera has a CCD array of 1008×1008 pixels. Each pixel has a square shape of 9 μm in length with a effective fill factor of 55%. The Megaplus 1.0 camera has an embedded secondary diode array that is able to store the electric charge collected by the CCD array. In other words, the diode array works as an in-board memory that is able to store a full frame while the CCD is collecting a completely new frame. There is an elapsed time gap from the end of light collection in the CCD and the charge transfer to the diode array. The minimum time needed to transfer the electric charge from the CCD to the secondary diode array is 5 μs for this particular camera.

The camera was configured via interface software to operate in the trigger double-exposure mode. In this mode of operation, the camera is able to acquire two consecutive images with a small time delay between them. The only restriction using this mode is that usually the first image has to be exposed for less than 1 ms while the second image has a fixed exposure time of about 32 ms. The trigger double-exposure feature of this camera allows it to take pictures up to 60 frames/s when accurately synchronized.

The first exposure time was reduced to the minimum 0.128 ms allowed. The camera then needs 0.005 ms to transfer the first image from the CCD array to a secondary diode array located inside the camera, enabling the acquisition of the second image with the now empty CCD array. While the acquisition of the second image is in progress, the information contained in the secondary diode array is transferred to the frame grabber hosted in a personal computer via a 128 pin cable.

E. Software

A program code written in LABVIEW was made to manage the incoming data generated in the camera. The program code manages the data acquisition and transfers process from the camera to the hard disk of the host computer. It also generates the adequate pulses that serve as a trigger for the pressure transducer acquisition. Basically, this program waits for the trigger signal generated by the frame grabber (National Instruments model PCI 1424) and then starts the acquisition of data. The program has the capability to choose the acquisition rate.

The maximum number of images, pressure raw data, and shear stress data in a single sequence is limited by the on board computer random access memory (RAM) and data transfer capabilities. A gigabyte of RAM is used for the computer host, allowing hundreds of images to be stored and transmitted to the hard drive in a small time.

To summarize the synchronization process, we can start with the high-accuracy pulse generator. The pulse generator generates an internal signal that is used as the time reference for all the acquisition process. The TTL pulses generated at channels A and C trigger the laser lamps with a time delay between them specified by channel B. Channel D triggers the acquisition of the high-resolution camera. The acquisition software for the high-resolution camera triggers the acquisition of pressure data at the same time that triggers the acquisition software of the optical shear stress sensor. Figure 7 shows the time diagram of the synchronization process.

III. RESULTS AND DISCUSSION

The tests were carried out with various volumetric water flow rates to achieve various Reynolds numbers. The Reynolds number (Re_h) is calculated using the half height of the channel, the bulk velocity, and the viscosity of water. The following section presents the results for $\text{Re}_h \cong 5128$. Two-phase flow measurements with various void fraction values were obtained. The average bubble size was 30 μm. The void fraction value within the measurement zone was estimated using the following relation:

$$\alpha = \frac{V_g}{V_g + V_l}, \tag{3.1}$$

where V_g is the volume of the gas bubbles in the viewing volume with thickness of about 1 mm and V_l is the volume of liquid in the viewing volume. In other words, the local

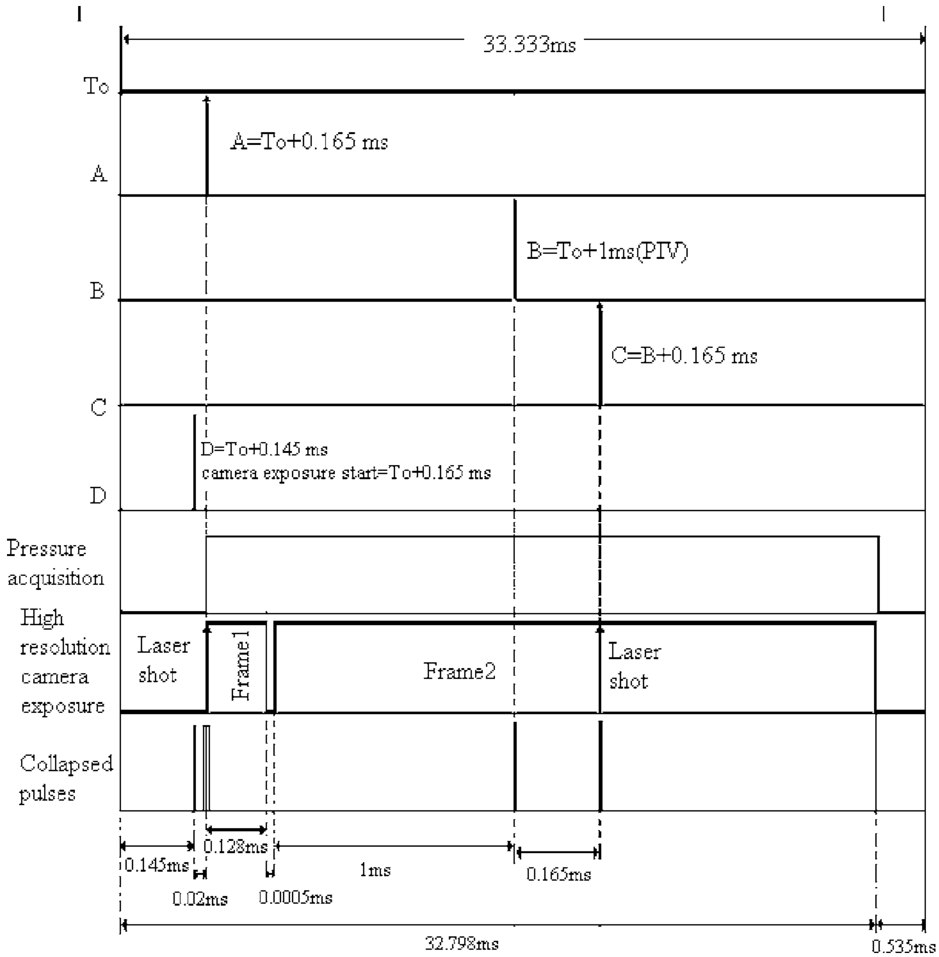

FIG. 7. Time frame system synchronization. T_0 is generated by the internal clock of the pulse generator. Channels A and C trigger the laser lamps. The synchronized acquisition of pressure data and PTV data starts with the trigger signal at channel D.

void fraction is calculated by identifying the microbubble present in the PTV images and relating this information to the amount of liquid present at the PTV measurement volume.

In this study, the particle tracking routine is a cross correlation algorithm. Two different software applications are used for the tracking process. The resulting velocity vectors from each application are then compared and combined. This hybrid tracking technique greatly increases the total number of velocity vectors used for the flow field analysis. One software allows online image processing and tracking of the particle tracers.[16] Thus, the image threshold and tracking parameters can be correctly set for a whole data set. This program is considered robust and reliable in particle centroid determination and tracking. The other tracking program and particle centroid determination algorithm were developed at Texas A&M University.[17] These algorithms have been improved over the years.

A. PTV analysis

Once the velocity vectors are obtained from both particle tracking algorithms, they undergo a filtering process. Statistical filters are applied independently to the vector data sets from each tracking process. The first filter was the cross correlation value itself. In our case, only those vectors with a cross correlation coefficient value higher than the average value, sometimes minus a standard deviation, of a whole vector data set are considered for the flow field analysis. Some of the rejected vectors can easily be seen as erroneous vectors. They are vectors with direction and/or magnitude far deviated from their neighbors. The second filter function removes vectors that are not within the average plus or minus a standard deviation value from the magnitude and direction of the representative velocity vector in a small window. This step ensures that velocity gradients are correctly delineated. In this step about 10% of the vectors are removed. Finally, the remaining vectors from each process are analyzed separately to obtain instantaneous velocity fields. Space- and time-averaged velocity fields are calculated in order to obtain statistical parameters of the flow. A typical time-averaged velocity field is shown in Fig. 8. The contour color plot elucidates the magnitude of velocity gradients present at the boundary layer.

TABLE I. Summary of two-phase flow cases studied. The average friction velocity decreases with increasing local void fraction.

Experiment	u_τ (m/s)	d^+	Void fraction α (%)	Drag reduction (%)
Single phase	0.0116	⋯	⋯	⋯
Case 1	0.0108	0.32	2.40	12
Case 2	0.0106	0.31	3.40	16
Case 3	0.0097	0.29	4.40	28
Case 4	0.0091	0.27	4.90	38

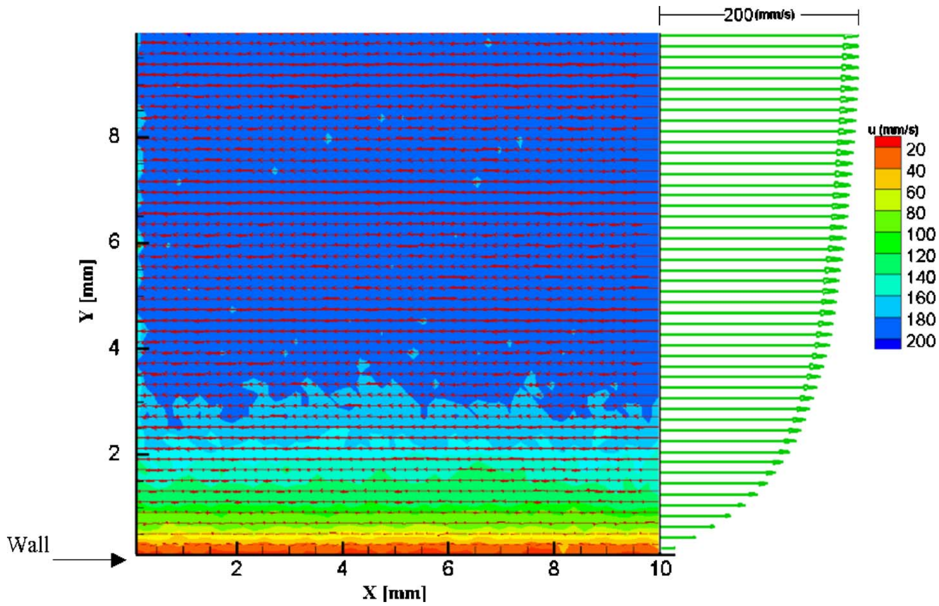

FIG. 8. (Color online) Typical time-averaged velocity field and its corresponding velocity profile, Re=5128, obtained from particle tracking velocimetry single-phase case.

The average number of instantaneous velocity vectors within the viewing area of approximately 1 cm^2 is about 1500. Instantaneous velocity vector fields are interpolated by applying the inverse distance algorithm using windows of 20×20 pixels. As a result of the interpolation process, the final instantaneous velocity fields have a vector distribution of 50×50 vectors. Once the vectors are distributed in the regular interpolation mesh (50×50), the viscous component of the total shear stress can be determined from the measured streamwise velocity profile. The derivative dU/dy was calculated using the central difference scheme.

The conditions of the various void fraction test cases for the $\mathrm{Re}_h \cong 5128$ case are summarized in Table I. These results confirm that drag reduction has a strong dependence on the local void fraction values. The average bubbles' diameter, d^+ is presented in wall units, in which friction velocity u_τ is calculated from Eq. (3.2).

The nondimensional d^+ is computed from Eq. (3.3). Comparison between the length scales present within the boundary layer and the nondimensional bubble size is important from the physical mechanism point of view in this regime,

$$u_\tau = \sqrt{\frac{\tau_w}{\rho}}, \tag{3.2}$$

$$d^+ = \frac{du_\tau \rho}{\mu}. \tag{3.3}$$

B. Optical sensor

Figure 9 shows typical burst outputs obtained from the optical shear stress sensor for single-phase flow and the case with microbubble injection. The X axis shows the nondimensional time and the Y axis shows voltage. It can be seen that the shape of the output is similar for both cases but the burst's amplitude changes. Irregularities at the beginning and the end of the output burst can be noticed for the case when the microbubbles are injected. Light scattering of the microbubbles causes these irregularities. It is of considerable concern to distinguish between bubbles and the seeded particles in the flow. Since microbubbles and particles can cross the measurement volume of the shear stress sensor, the analysis of the result is based on the different effect of the microbubbles and seeds. This effect was obtained based on a discriminating factor. This factor is obtained based on the fact that microbubbles and the seeded particles have a different refractive index and bubbles scatter light in a different way than a tracer particle. Comparison of the amplitude of the output burst from the shear stress sensor when only the seeded particles are present in the flow against the burst am-

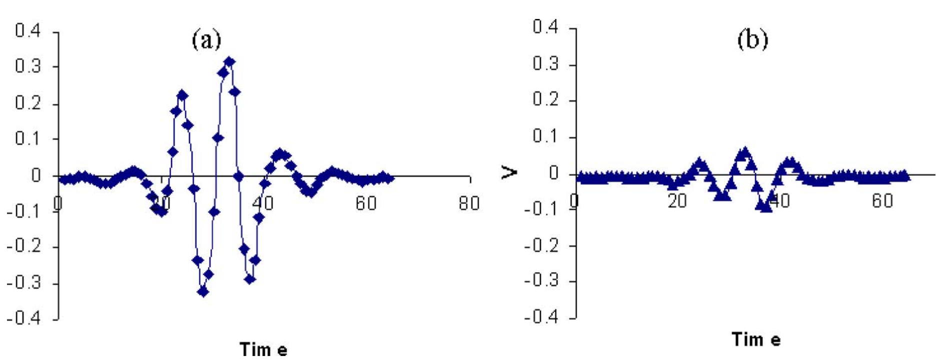

FIG. 9. (Color online) Typical voltage burst output from the divergence fringe Doppler sensor after filtration for (a) single-phase flow (b) two-phase flow. There is a change in signal amplitude that helps to discern between bubbles and tracer particles crossing the measurement volume.

TABLE II. Statistical results from the optical shear stress sensor.

Re=5128	Mean (Hz)	Median (Hz)	Mode (Hz)	$\sqrt{\overline{u'^2}}$ (Hz)
Single phase	2269	2258	2274	480
Two phase	2040	1994	2116	396

TABLE III. Average wall shear stress measured with the optical sensor.

Re=5128	τ_w (Pa)	Drag reduction (%)
Single phase	0.15	
Two phase	0.135	10

plitude when only microbubbles are present in the flow yields a characterization of the output bursts.

The importance of removing the burst generated by the microbubbles relies on the fact that the need is to determine the velocity of the fluid phase and not the velocity of the gas phase. Once the bursts have been obtained for the different data sets, a power spectrum algorithm based on the application of the fast Fourier transform was used to extract the characteristic frequency of each burst. This frequency determines the velocity in hertz of particles crossing the Doppler fringes within the measurement volume.

Table II summarizes the results obtained from the shear stress sensor. A reduction in the wall shear stress when the microbubbles are injected is noticed. Table III presents the wall shear stress measured in pascals. These results were obtained with a local void fraction of 2.4%, since the sensor performance decreases considerably when higher local void fractions were present at the measurement zone. The cause for this decrease is the eventual attachment of some microbubbles to the top channel wall, which in turn changes the measuring conditions explained before for optimal performance of the sensor.

C. Pressure transducer

The measured value of pressure drop can be transformed to its corresponding value of wall shear stress using Eq. (2.1). The continuous pressure signal was sampled at a frequency rate of 1000 Hz to obtain a discrete representation of the differential pressure fluctuations. Figure 10 shows a typical output of the discretized pressure signal for single-phase and two-phase flows. The Y axis represents the calculated wall shear stress with the pressure drop in pascals, and the X axis represents the acquisition time. Once again, the pressure signal shows a decrease in the wall shear stress when the microbubbles are injected within the boundary layer of the channel flow. The nature of the pressure fluctuations indicates changes in the wall pressure that in turn could be related to the turbulence structures in the fluid. The average wall shear stress values obtained with a local void fraction of 2.4% are listed in Table IV.

D. System verification

Table V shows the results of the wall shear stress using the three methods for single-phase flow and with microbubble injection for a local void fraction α=2.4%. In this study, the three methods proposed for quantification of drag reduction are shown to be in good agreement (see Table V). All of them showed a decrease in the wall shear stress when the microbubbles were injected into the boundary layer of the turbulent flow. An average drag reduction of 10% was observed for local void fractions of 2.4% by the three methods. The agreement of the various techniques for measurement of wall shear stress narrows the possibility of error inherent to every measurement system by direct comparison of the sensors readings.

The data output format is characteristic to each measurement technique. The PTV technique (after processing) gives instantaneous velocity measurements of 2500 spatial positions, which in turn are used to calculate the wall shear stress. Hence, one value of wall shear stress can be calculated from every velocity field. The frequency resolution of these measurements is limited by the maximum acquisition frame rate of the PTV system which is 60 frames/s, resulting in a maximum frequency response of 30 Hz (two frames are needed to obtain one velocity field). Thus, PTV brings up the possibility to observe the velocity flow behavior at 2500 simultaneous positions every 33.3 ms. The frequency and spa-

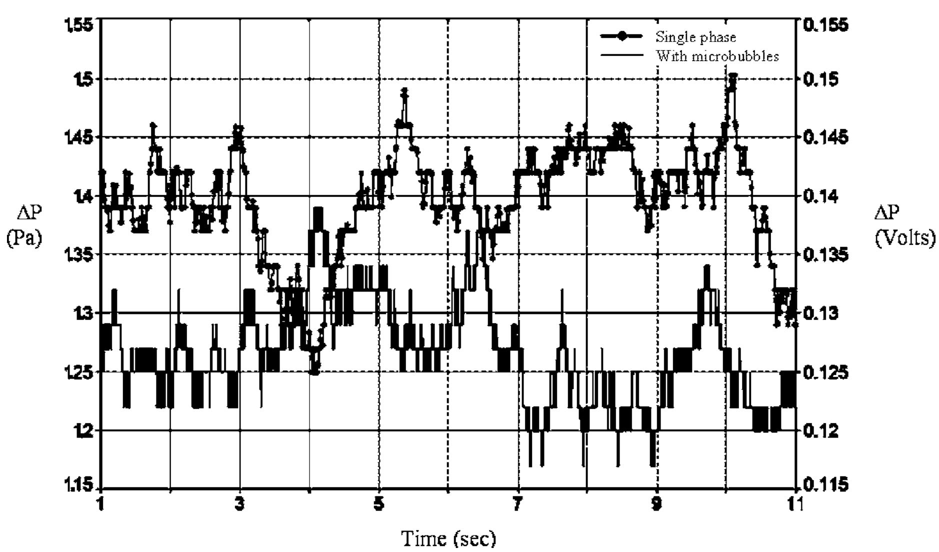

FIG. 10. Differential pressure vs time, Re=5128, typical pressure signal without filtering for single and two-phase flow.

TABLE IV. Average wall shear stress calculated from the wall pressure drop.

Re=5128	τ_w (Pa)	Drag reduction (%)
Single phase	0.16	
Two phase	0.144	10

TABLE V. Comparison of the obtained wall shear stress by the three methods.

	Method		
Re=5128 $\alpha=2.4\%$	PTV $\tau_w=-\mu\frac{\partial u}{\partial y}$ (Pa)	Optical Sensor $\tau_w=-\mu(f\times k)$ (Pa)	Pressure Drop $\tau_w=-H\frac{\partial P}{\partial x}$ (Pa)
Single phase	0.15	0.15	0.16
Two phase	0.13	0.13	0.14

tial resolution are characteristics inherent to the PTV system and they are not affected by the microbubble injection.

The optical sensor gives wall shear stress point measurements. Although its spatial resolution is just one position, its frequency response can be in the megahertz range. The frequency response is basically delimited by the photodetector response. Nevertheless, there must be particles crossing the measurement volume in order to obtain a measurement, so, in our case, the frequency response of this sensor is delimited by the rate of particles crossing the measurement volume. For the Reynolds number studied, the frequency response is in the kilohertz range. This response is diminished when microbubbles are injected in the flow. The decrease is a consequence of the fact that bubbles and tracer particles are crossing the measurement volume. In addition, the buoyancy forces exerted on the bubbles lead to its eventual attachment to the wall. Bubble attachment caused two main problems with the optical sensor: the obstruction of the flow aiming the optical sensor measurement volume or the direct attachment of the bubble to the sensor's surface. For both cases, the performance of the sensor is affected by decreasing its time response. The sensor performance is not considerably affected when the local void fraction does not exceed 2.4%.

Measurements from the pressure transducer are considered as point measurements. The frequency response of this sensor is in the hundreds of hertz range. Its response is limited by the diaphragm displacement and piping characteristics. The frequency response is not affected when microbubbles are injected in the flow. Since the transducer's output is a continuous voltage function linear to the pressure drop value, the fluctuations in the wall shear stress are easily observed in the response function. The sensor's output shows a decrease in wall shear stress when microbubbles are injected in the flow. The average decrease in wall shear stress measured with the pressure transducer agrees with PTV and the optical sensor for local void fractions of 2.4%. However, even when the local void fraction was increased up to 4.9%, the sensor's average response indicates about the same value. It is important to notice that the structure of the output signal is not the same when the higher local void fractions are tested, but its average value is still without considerable change.

The agreement of the three measurement techniques can be quantified by observing the obtained values in Table V. There is a 93% agreement in the average wall shear stress measurements for the single-phase flow case and 92.8% for the two-phase flow case. The particle tracking velocimetry technique elucidates a higher drag reduction of as much as 38% for a local void fraction of 4.9% when microbubbles are injected within the boundary layer of the channel flow. These results are exclusive to the PTV technique, since the optical sensor performance diminished with local void fractions higher than 2.4% and the pressure transducer average response shows no appreciable change for the rest of the local void fractions tested. The synchronized measurement system offers the possibility to correlate data from the three measurement techniques. This capability may bring insight about the complex phenomena present in two-phase flow boundary

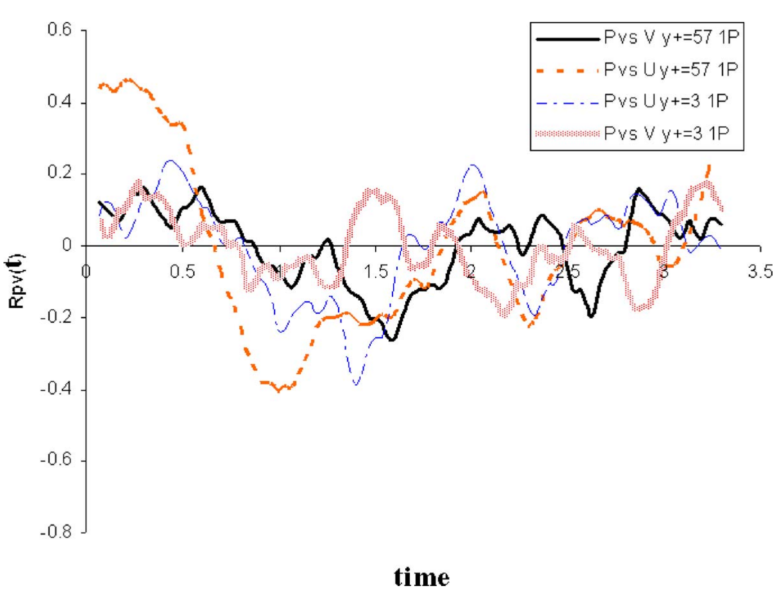

FIG. 11. (Color online) Cross correlation coefficient vs time for single-phase flow, Re=5128. Two distances from the wall are chosen, $y^+=3$ and $y^+=57$, from the PTV data. Synchronized measurements of pressure difference and both components of the velocity vector are correlated. There is a high correlation of pressure measurements and the streamwise component of the velocity vector.

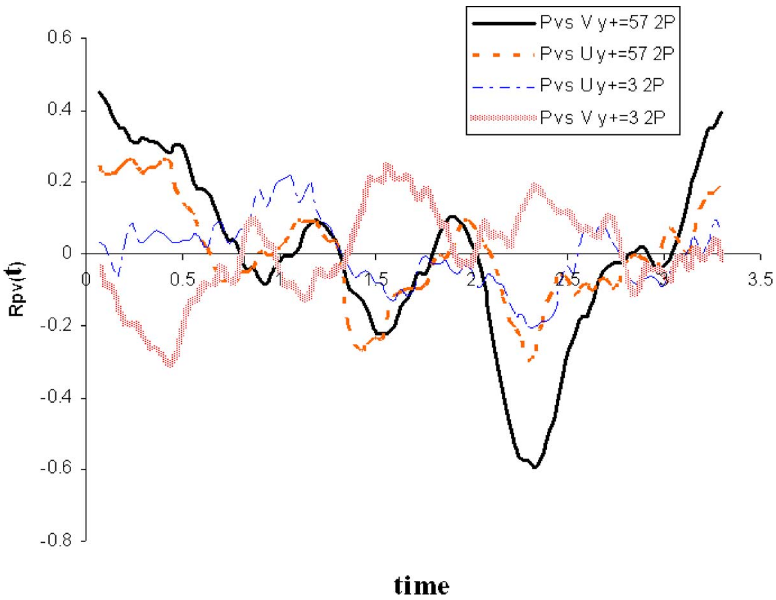

FIG. 12. (Color online) Cross correlation coefficient vs time for two-phase flow (α=2.4%), Re=5128. Two distances from the wall are chosen, y^+=3 and y^+=57, from the PTV data. There is a high correlation of pressure measurements and both components of the velocity vector.

layers. Figure 11 shows the results of pressure data correlated with PTV data. The data were acquired using the integral measurement system in the channel flow described previously for a Re=5218 and α=2.4%. Velocity and pressure difference fluctuations were calculated by subtracting the mean to each value of the sample. Then, a standard cross correlation algorithm was applied to the fluctuating signals. In order to correlate pressure data to PTV data, the former has to be in some way averaged over space to compensate for the inability of the pressure measurements to have spatial resolution of the same order. This is achieved by performing spatial averaging from the PTV data in the streamwise direction (parallel to the channel's wall). In this way there is only one velocity vector at a certain distance from the wall that is correlated with one pressure difference discrete value. It can be seen in Fig. 11 that the pressure measurements correlate high with the streamwise component (u) of the velocity vector for the single-phase case (triangular markers). The correlation coefficient is about half its value when the pressure is correlated with the spanwise (v) component of the velocity vector for the single-phase case. The cross correlation value changes when microbubbles are injected within the boundary layer of the channel flow (see Fig. 12). In this case, the value of the cross correlation coefficient increases when the pressure is correlated with the spanwise component of the velocity vector. These results suggest that there is a modification of the flow natural structure when the microbubbles are injected. The ability to correlate data acquired at the same time has a potential to further clarify the role of shear stress in two phase flows.

IV. ERROR ANALYSIS

A. Particle tracking velocimetry

The uncertainty in the velocity measurements obtained using PTV is a direct consequence of a combination of errors from two main sources. These are the localization of the centroid of the seed particle and microbubble images and their displacements in the two-dimensional (2D) images and the uncertainty of how well the tracer particles follow the actual fluid motion. This last uncertainty can be determined utilizing the particle Stokes number, which is calculated as the ratio of the relaxation time of the seed particle to the characteristic time of the flow. The particle relaxation time τ_p, also known as the momentum or velocity response time, is the time needed by a seed particle to reach the value $e^{-1}U$, if the particle was initially at rest. Here U is the fluid velocity. The time τ_p can be computed from

$$\tau_p = \frac{(2\rho_p + \rho_f)d_p^2}{36\mu_f}, \tag{4.1}$$

where ρ is the density, d the seed tracer diameter, μ the viscosity, and the subscript p refers to particle properties and f to the fluid properties. In this experiment, $\rho_p = 1050\ \text{kg/m}^3$, $\rho_f = 1000\ \text{kg/m}^3$, $d_p = 6\times10^{-6}$ m, and $\mu_f = 1002\times10^{-6}\ \text{kg/(m s)}$. Thus, the relaxation time of the seed was calculated to be 3.0 μs.

The fluid time scale τ_f is the time needed by the fluid to be advected within a characteristic length L at a velocity U, that is,

$$\tau_f = \frac{L}{U}. \tag{4.2}$$

To compute the characteristic time of the flow, the seed tracer mean diameter and the average cross sectional velocity of the liquid were used. The resultant fluid time scale is 77.7 μs. Then, the resulting Stokes number, τ_p/τ_f, is 3.9×10^{-2}. Therefore, the 6 μm seed particles closely followed the fluid motion changes and therefore did not significantly contribute to the total error.

The major source of error in the PTV system is the uncertainty in determining the centroid of the spot images of both the tracer particles and microbubbles. The error in locating the centroid displacements depends on the optical parameters of the camera, lenses, and laser and the algorithm for finding the particle image centroid. Two different software applications were used for spot centroid finding and particle tracking. The first software utilizes a subpixel accuracy algorithm where the centroid is located using modified weighting factors. In the second software, the centroid is computed using the center of mass location method by weighing every pixel with the value of its intensity, that is, if $I(x,y)$ is the gray scale pixel intensity at the position (x,y) on a tracer seed particle or microbubble spot image, the center of mass location is given by

$$(x_0,y_0)_{\text{center of mass}} = \frac{\sum_{\text{spot area}} (x,y) \times I(x,y)}{\sum_{\text{spot area}} I(x,y)}. \quad (4.3)$$

The centroid in this case is called the first order moment. This algorithm requires a precise determination of the spot image border. This kind of algorithm has typical errors smaller than 0.01 pixel for simulated ideal particle images. However, the error increases as the noise increases and the spot image size decreases. By using calibration images, a rms error of 0.1 pixel in calculating the particle image centroids was determined. This error was assumed as the overall error of the measurements, although the other algorithm had a rms error of 0.25 pixel.

The uncertainty of the components of the velocity vector can be computed through the error propagation formula. This relationship assumes that if the errors associated with a measurement are small and symmetric around zero, the uncertainty associated with any quantity, σ_s, derived from, for example, three measurements is given by

$$\sigma_s^2 = \left(\frac{\partial s}{\partial r_1}\right)^2 \sigma_{r1}^2 + \left(\frac{\partial s}{\partial r_2}\right)^2 \sigma_{r2}^2 + \left(\frac{\partial s}{\partial r_3}\right)^2 \sigma_{r3}^2, \quad (4.4)$$

where r_1, r_2, and r_3 are the values of the measurements and σ_{r1}, σ_{r2}, and σ_{r3} are their respective associated errors. Thus, to calculate the uncertainty of the components of the instantaneous velocity vectors $\mathbf{U}=\mathbf{U}(U,V)$, we first note that the velocity components are calculated from the subtraction of the coordinates of the position vector $\mathbf{X}=\mathbf{X}(x,y)$ divided by the time interval between laser pulses, Δt. Thus, using Eq. (4.4), the rms error value of 0.1 pixel implies an error of 0.28 pixel in the calculation of the particle image centroids for the two particle images needed in calculating the displacement. In terms of velocity units, the rms error is then 1.02 mm/s for each velocity component. This value is determined considering negligible error in the time separation between frames (1 ms) and the 0.1 pixel error of the particle image displacement.

The velocity gradient dU/dy was computed from the average value of the U component at each different y position. Therefore, the uncertainty of dU/dy relates to that of $\bar{U}$, which, in turn, comes from the error of the instantaneous values of U. The uncertainty σ associated with the components of the mean velocity vector $\bar{\mathbf{U}}=\bar{\mathbf{U}}(\bar{U},\bar{V})$ can be calculated, using again Eq. (4.4), from

$$\sigma_{\bar{U},\bar{V}} = \frac{\sigma_{U,V}}{\sqrt{n}}, \quad (4.5)$$

where n is the total number of samples employed in the average calculation. The value of n was 1000. Thus, $\sigma_{\bar{U},\bar{V}}=0.025$ mm/s. The error associated with the central difference algorithm must be added to the obtained value which gives a total result of $\sigma_{\bar{U},\bar{V}}=0.025+0.1=0.125$ mm/s. This is a top value for the uncertainty in the calculation of dU/dy. It can, finally, be calculated that the maximum error in the calculation of the wall shear stress is about 4.5%.

B. Optical sensor

The main sources of error in the optical sensor are the tracer particle ability to accurately follow the flow behavior, location of the measurement volume outside the quasilinear sublayer of the boundary layer, and erroneous particle identification.

The tracer particles for the optical sensor are the same particles utilized in the PTV system. The relaxation time and time scale of the seeded particles were calculated previously in the section above and it is concluded that the error produced by the tracer particles is small so that it can be neglected. The positioning of the measurement volume of this sensor greatly depends on its physical positioning at the channel wall. Photographic inspection with resolution of 10 μm revealed that the sensor surface was located at a distance of 190 μm from the channel's interior surface. Considering the smallest friction velocity measured by the three methods exposed in this work (8 mm/s), the corresponding distance in wall units of the sensor's surface is $y^+=1.5$ which is less than 5. Hence the sensor's associated error can be neglected. Spurious particles crossing the measurement volume such as impurities in the fluid or gas bubbles may produce erroneous velocity measurements. The associated uncertainty was determined experimentally being less than 1%. The total error of the optical sensor system is estimated using the statistical standard deviation from the measured data. This value comes to be 6.5%.

C. Pressure sensor

For variable reluctance pressure sensors, the only mechanical part that moves in response to pressure is the sensing diaphragm, and the total displacement over a full-scale pressure excursion is less than two-thousandths of an inch. There are no mechanical linkages or hydraulics inside the sensor to slow down the sensing element. The position of the diaphragm is measured inductively, and this is how the sensed pressure is converted to an electrical signal. The major sources of error for this sensor are the accuracy of the analog/digital converter used to sample the analog signal and the possibility of electric noise induced to cable connectors or the sensor itself. The board used to capture the analog signal coming from the sensor has a 12 bit resolution which leads to 4096 discrete or digital levels. The full-scale range of the transducer is 5 V; therefore the minimum resolution level is of 1.2 mV or 0.02% of error. The noise induced to the connectors and the sensor was assumed to be white noise or Gaussian, since the all the connectors used are shielded connectors with coupled impedance. Hence, the error induced can be neglected. The total error associated with this sensor will be taken from the fabricant specifications which in this case is 0.025% of the full scale.

V. DISCUSSION

The methods used to measure the wall shear stress offer complementary information for the understanding of the drag reduction phenomena. However, each method has its own advantages and disadvantages.

The PTV system used in this study has the advantage of an acceptable spatial resolution but poor temporal resolution. In addition, the PTV technique performed satisfactory for the various void fractions studied. The optical shear stress sensor has the advantage of great time resolution but a poor spatial resolution. The frequency response of this system could reach the megahertz range, although its spatial resolution is limited since it measures the wall shear stress at a specific location. The optical sensor proves to be in good agreement with the expected values of wall shear stress for single-phase flow. However, the optical sensor shows operational limitations for local void fractions higher than 2.4%.

Finally, the wall pressure measurement method has the advantage of a good sensitivity but a poor time resolution. The wall pressure gradient measurements proved to be a reasonable tool for the measurement of drag reduction. As opposed to the PTV and the optical sensor, this method does not require the flow to be seeded with external particles. Values of the instantaneous wall shear stress can be obtained by direct observation of the pressure signal, which could help in the design of systems capable of controlling the skin friction based on a feedback given by the wall pressure signal. The system's capability to directly relate data from other sensors to the PTV acquired velocity fields brings insight about the complex phenomena involved in turbulent boundary layers disturbed with microbubbles.

ACKNOWLEDGMENT

The authors would like to thank Michael Kotas for his efforts and fruitful discussions during this study.

[1] D. B. Macvean and S. Aly, J. Phys. E **11**, 1048 (1978).
[2] S. Haasl, D. Mucha, V. Chernoray, T. Ebefors, P. Enoksson, L. Löfdahl, and G. Stemme, J. Microelectromech. Syst. **14**, 254 (2005).
[3] R. Mayer, R. A. W. M. Henkes, and J. L. Ingen, Int. J. Heat Mass Transfer **41**, 2347 (1998).
[4] F. J. H. Gijsen, A. Goijaerts, F. N. Van De Vosse, and J. D. Janssen, J. Rheol. **41**, 995 (1997).
[5] D. Bocchiola, G. Menduni, and D. Ward, J. Hydraul. Eng. **129**, 102 (2003).
[6] M. E. Mccormick and R. Bhattacharyva, Nav. Eng. J. **85**, 11 (1973).
[7] G. S. Migirenko and A. R. Evseev, *Turbulent Boundary Layer with Gas Saturation* (Nauka, Novosibirsk, 1974), p. 132.
[8] V. G. Bogdevish and A. R. Evseev, *Effect of Gas Saturation on Wall Turbulence* (Thermophysics Institute Publishing House, Novosibirsk, 1976).
[9] N. K. Madavan, C. L. Merkle, and S. Deutsch, J. Fluids Eng. **107**, 370 (1985).
[10] A. A. Fontaine, S. Deutsch, T. A. Brungart, H. L. Petrie, and M. Fenstermacker, Exp. Fluids **26**, 397 (1999).
[11] M. M. Guin, H. Kato, H. Yamaguchi, M. Maeda, and M. Miyinaga, J. Mar. Sci. Technol. **1**, 246 (1996).
[12] S. Fujikawa, R. Zhang, S. Hayama, and G. Peng, Int. J. Multiphase Flow **29**, 1221 (2003).
[13] J. Ortiz-Villafuerte and Y. A. Hassan, J. Fluids Eng. **128**, 507 (2006).
[14] M. Gharib, D. Modarress, D. Fourguette, and D. Wilson, 40th AIAA Aerospace Sciences Meeting and Exhibit, Reno, NV, 2002 (available at http://www.viosense.com/publications.shtml).
[15] D. Fourguette, D. Modarress, D. Wilson, M. Koochesfahani, and M. Gharib, 31st AIAA Fluid Dynamics Conference and Exhibit, Anaheim, CA, 2001 (available at http://www.viosense.com/publications.shtml).
[16] T. Uemura, F. Yamamoto, and K. Ohmi, *Application of Laser Techniques to Fluid Mechanics* (Springer, Berlin, 1991).
[17] Y. A. Hassan, T. K. Blanchat, C. H. Seeley, Jr., and R. E. Canaan, Int. J. Multiphase Flow **18**, 371 (1992).